

Research Article

Scheimpflug Camera-Based Stereo-Digital Image Correlation for Full-Field 3D Deformation Measurement

Cong Sun ^{1,2}, Haibo Liu ^{1,2}, Yang Shang ^{1,2}, Shengyi Chen,³ and Qifeng Yu^{1,2}

¹College of Aerospace Science and Engineering, National University of Defense Technology, Changsha 410073, China

²Hunan Provincial Key Laboratory of Image Measurement and Vision Navigation, Changsha 410073, China

³China Satellite Maritime Tracking and Control Department, Jiangyin 214431, China

Correspondence should be addressed to Haibo Liu; liuhaibo@nudt.edu.cn

Received 10 October 2019; Accepted 28 November 2019; Published 17 December 2019

Academic Editor: Manuel Aleixandre

Copyright © 2019 Cong Sun et al. This is an open access article distributed under the Creative Commons Attribution License, which permits unrestricted use, distribution, and reproduction in any medium, provided the original work is properly cited.

To further extend the scope of stereo-digital image correlation (stereo-DIC) to more challenging environments, a novel Scheimpflug camera-based stereo-DIC is developed for full-field 3D deformation measurement, wherein the Scheimpflug condition, consisting of tilting the sensor plane with respect to the lens plane for the sake of larger depth of field (DOF) of the camera, is employed. The geometric imaging model of the Scheimpflug camera is described, on the basis of which a robust and effective stepwise calibration strategy is performed to calculate the intrinsic and extrinsic parameters of the stereo Scheimpflug rig. With the aid of a specially tailored stereo triangulation method and well-developed subset-based DIC algorithms, the three-dimensional shape and displacement of the specimen can be retrieved. Finally, practical experiments, including rigid motion tests and three-point bending tests, demonstrate the effectiveness and accuracy of the proposed approach.

1. Introduction

Since Kahn-Jetter and Chu [1] and Luo et al. [2] laid the foundation and established the main framework based on image correlation and stereovision in the early 1990s, stereo-DIC has been significantly improved in the aspects of accuracy, computational efficiency, and robustness [3, 4]. Actually, stereo-DIC has evolved into a quite mature noncontact image-based optical technique for full-field 3D shape, displacement, and deformation measurements. Due to its outstanding superiorities, stereo-DIC has been extensively adopted in various fields, ranging from regular metal to composite materials [5] or even biological tissues [6], from nano- [7] to macroscopic scale [8], from static or quasistatic loading to high-speed dynamic loading [9], and from laboratory conditions to industrial extreme environments [10].

Nevertheless, the application of stereo-DIC might be constrained in view of the limited field of view (FOV) in the required working distance. In order to deal with the challenge, multicamera stereo-DIC, in which three or more cameras are employed to capture the surface images of the

specimen from multiviews, has been developed [11–14]. Generally, the multi-DIC system can be regarded as a combination of multiple regular stereo-DIC systems, firstly each stereo-DIC measures the local 3D shape at different regions of the specimen surface, and then the obtained results via individual stereo-DIC are stitched or mapped to the universal reference system with precalibration parameters. In spite of the fact that the multi-DIC system produces a sufficiently larger effective FOV, the uncertainty of the system might increase and the robustness deteriorates with the growth of the camera number. Moreover, multicamera calibration with high precision and flexibility is still a challenging problem.

In this work, an alternative approach of the Scheimpflug camera-based stereo-DIC method is provided. The Scheimpflug camera, adopting the Scheimpflug condition by tilting the lens with respect to the image plane, enables extending the measurement range of the stereo-DIC system without zooming the aperture, which has been widely employed in the field of particle image velocimetry (PIV) [15], line structured light [16], and portable 3D laser scanner [17].

However, to the best of our knowledge, Scheimpflug cameras have been rarely involved in stereo-DIC literatures so far.

The outline of the paper is as follows. Section 2 elaborates the geometric imaging model including lens distortion of the Scheimpflug camera, on the basis of which a robust and effective stepwise calibration strategy is presented to calculate the intrinsic and extrinsic parameters of the stereo Scheimpflug rig. In Section 3, the tailored Scheimpflug stereo triangulation method and well-developed subset-based DIC algorithms utilized in this work are introduced in detail. For validation, practical experiments, including rigid motion tests and three-point bending tests, are performed in Section 4 to evaluate the performance of the proposed method. Finally, brief conclusions are drawn in Section 5.

2. Scheimpflug Camera Model and Stereo Calibration

2.1. Scheimpflug Camera Model. As depicted in Figure 1(a), the Scheimpflug principle, traditionally credited to Theodor Scheimpflug in 1902, states that the object plane (the plane that is in focus), the thin lens's plane, and the image plane must all meet in a single line, the Scheimpflug line [18, 19]. The principle is applicable to both thin prism and thick prism models, with minor corresponding modifications. To ensure its further high-quality measurement in stereo-DIC systems, accurate calibration of the Scheimpflug stereo rig is the prerequisite and most essential step. Yet the conventional calibration methods are not valid in this case because the assumptions used by classical calibration methodologies are not satisfied anymore for cameras undergoing the Scheimpflug condition [20]. Therefore, more and more researchers devote themselves to the related research, and a variety of methods have been proposed to accommodate various applications [21–25]. Inspired by the conclusion drawn in literature [26], the Scheimpflug imaging model based on RMM (rotation matrix model) is adopted in this section.

RMM models the lens-image sensor configuration by an explicit rotation matrix about the optic axis and includes it as a part of the intrinsic calibration parameter set. As illustrated in Figure 1(b), $O-X_C Y_C Z_C$ is the camera coordinate system with the origin at the optical center, while the intersection $O(Cx, Cy)$ of the optical axis Z_C with the ideal image plane I_O is referred to as the principal point. Denoted as $O-x_t y_t$, the image coordinate system of the tilted Scheimpflug image plane I_S shares the same origin with the $O-xy$ in the image plane I_O . And the symbols α and β indicate the rotational angles about axes X_C and Y_C , respectively. The 3D world point $P_W(X_W, Y_W, Z_W)$ projects on I_O at point $p_i(x, y)$, and the light ray intersects I_S at point $p_t(x_t, y_t)$.

The conventional perspective projection can be briefly expressed as

$$\lambda \begin{bmatrix} p_i \\ 1 \end{bmatrix} = \mathbf{K} \begin{bmatrix} \mathbf{R} & \mathbf{T} \\ \mathbf{0} & 1 \end{bmatrix} \begin{bmatrix} P_W \\ 1 \end{bmatrix}, \quad (1)$$

where \mathbf{R} and \mathbf{T} indicate the rotation matrix and translation vector of the camera frame relative to the world frame,

respectively. Usually, extrinsic parameters $\{\gamma, \kappa, \theta, t_x, t_y, t_z\}$ refer to the three angle components defining the successive rotation about axes $\mathbf{R} = \mathbf{R}_X(\gamma)\mathbf{R}_Y(\kappa)\mathbf{R}_Z(\theta)$ and the three translation components. Besides, λ is the projective depth, and $\mathbf{K}_{3 \times 3}$ is the camera intrinsic matrix with respect to the ideal image plane, which is defined as

$$\mathbf{K} = \begin{bmatrix} fx & 0 & Cx \\ 0 & fy & Cy \\ 0 & 0 & 1 \end{bmatrix}, \quad (2)$$

where fx and fy denote the horizontal and vertical focal length in pixel units, respectively.

Taking the tilt effect of the Scheimpflug condition into account, the rotation which maps the plane I_O onto the plane I_S can be split into successive rotation about axes X_C and Y_C with angles α and β .

$$\mathbf{R}_S = \begin{bmatrix} \cos \beta & 0 & \sin \beta \\ 0 & 1 & 0 \\ -\sin \beta & 0 & \cos \beta \end{bmatrix} \begin{bmatrix} 1 & 0 & 0 \\ 0 & \cos \alpha & -\sin \alpha \\ 0 & \sin \alpha & \cos \alpha \end{bmatrix}. \quad (3)$$

Therefore, the projection p_t in the tilted Scheimpflug image plane of the world point P_W can be modeled as follows, and the detailed derivation process can be found in Reference [25].

$$\lambda_1 \begin{bmatrix} p_t \\ 1 \end{bmatrix} = \mathbf{K} \mathbf{A} \mathbf{R}_S^T \begin{bmatrix} \mathbf{R} & \mathbf{T} \\ \mathbf{0} & 1 \end{bmatrix} \begin{bmatrix} P_W \\ 1 \end{bmatrix}, \quad (4)$$

where λ_1 is the arbitrary scale factor and \mathbf{A} is the Scheimpflug array:

$$\mathbf{A} = \begin{bmatrix} \cos \alpha \cos \beta & 0 & \sin \beta \\ 0 & \cos \alpha \cos \beta & -\cos \beta \sin \alpha \\ 0 & 0 & 1 \end{bmatrix}. \quad (5)$$

Substituting Equations (1), (2), (3), and (4) and letting the normalized coordinates in I_O be denoted as $p_n(x_n, y_n)^T$, thus, the transformation that relates p_n to the image point p_t can be achieved.

$$\lambda_2 \begin{bmatrix} p_t \\ 1 \end{bmatrix} = \mathbf{K} \mathbf{A} \mathbf{R}_S^T \begin{bmatrix} p_n \\ 1 \end{bmatrix}. \quad (6)$$

Likewise, λ_2 is the arbitrary scale factor. In view of the inevitable lens distortion, the radial and tangential lens distortions are taken into account on the ideal image plane I_O [38].

$$\begin{aligned} x_d &= (k_1 r^2 + k_2 r^4) x_n + 2p_1 x_n y_n + p_2 (r^2 + 2x_n^2), \\ y_d &= (k_1 r^2 + k_2 r^4) y_n + 2p_2 x_n y_n + p_1 (r^2 + 2y_n^2), \end{aligned} \quad (7)$$

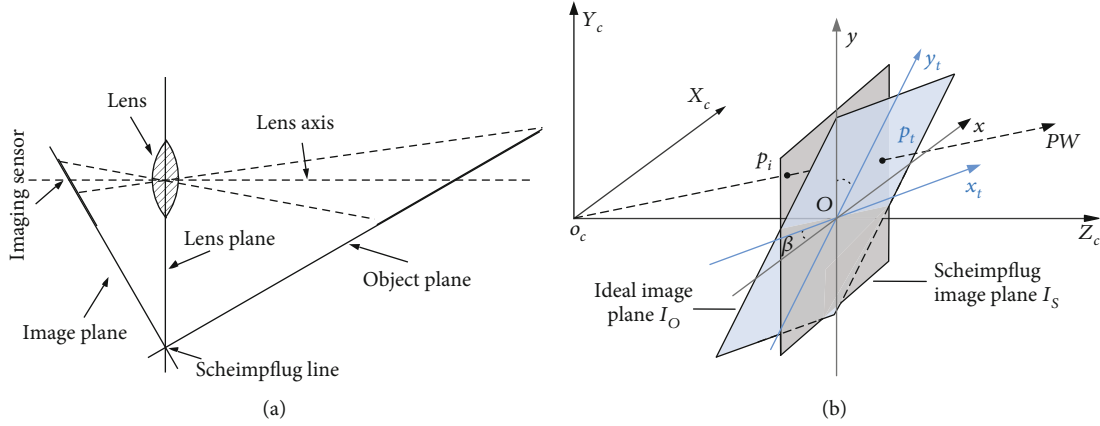


FIGURE 1: Schematic of the imaging system applied with the Scheimpflug principle: (a) Scheimpflug principle in a 2D view; (b) optical geometry of the Scheimpflug camera in a 3D view.

where $r^2 = x_n^2 + y_n^2$ and $(k_1, k_2), (p_1, p_2)$ represent the radial and tangential distortion coefficients, respectively. Thus, relying on Equations (1), (2), (3), (4), (5), (6), and (7), the Scheimpflug imaging model including lens distortion is established.

2.2. Stepwise Calibration of the Stereo Scheimpflug Camera. In consideration of the sensitivity and dependency of the Scheimpflug camera's parameters, the stepwise calibration strategy analogous to the literature [23] is employed to allow an adequate scope for parameter values. Besides, on account of the unique advantages of the planar calibration object, a planar checkerboard is adopted in this section. Sufficient images of the calibration object ought to be acquired by two cameras synchronously from multiple views.

A stereo rig composed of two Scheimpflug cameras is considered. As depicted in Figure 2, O_1 and O_2 are the optical centers of the left and right cameras, respectively. A 3D world point P projects on I_O^L at point p_i^L , the light ray intersects I_S^L at point p_t^L in the left images, and the camera baseline, respectively, intersects image planes I_O^L and I_S^L at e^L and e_t^L ; likewise, in the right images. Given all the calibrated intrinsic and extrinsic parameters of the stereo rig $(\alpha_g, \beta_g, K_g, R_g, T_g, g = L, R)$, we have

$$\lambda_L \begin{bmatrix} p_t^L \\ 1 \end{bmatrix} = \mathbf{K}_L \mathbf{A}_L \mathbf{R}_{LS}^T \begin{bmatrix} \mathbf{R}_L & \mathbf{T}_L \\ \mathbf{0} & 1 \end{bmatrix} \begin{bmatrix} P_W \\ 1 \end{bmatrix}, \quad (8)$$

$$\lambda_R \begin{bmatrix} p_t^R \\ 1 \end{bmatrix} = \mathbf{K}_R \mathbf{A}_R \mathbf{R}_{RS}^T \begin{bmatrix} \mathbf{R}_R & \mathbf{T}_R \\ \mathbf{0} & 1 \end{bmatrix} \begin{bmatrix} P_W \\ 1 \end{bmatrix}. \quad (9)$$

Supposing that a set of image correspondences $p_t^L \leftrightarrow p_t^R$ is given, then the corresponding world point set P_W can be calculated combining Equations (8) and (9).

In general, the stepwise calibration scheme of stereo Scheimpflug cameras can be divided into five consecutive steps.

Step 1. Initialization of the intrinsic and extrinsic parameters of the two individual cameras. In terms of intrinsic parameters, the Scheimpflug angles (α, β) can be roughly estimated according to literature [25] or just obtained from the data-sheet. Meanwhile, identical with the frequently used method, the principal point (C_x, C_y) is initialized at the center of the image plane. Furthermore, the distortion coefficients are assumed to be zero. For the extrinsic parameters $\Phi (\gamma^k, \kappa^k, \theta^k, t_x^k, t_y^k, t_z^k)$, they can be calculated from the homographies of all captured images using Zhang's method [20], without taking the Scheimpflug condition and lens distortion into account.

Step 2. Estimation of the Scheimpflug angles of two individual cameras. The projection from P_W to the Scheimpflug image plane, depending on Equations (1), (2), (3), (4), (5), (6), and (7), can be denoted by \tilde{p}_t . To estimate the Scheimpflug angles, the following objective function ρ is minimized:

$$\rho_i = \min \sum_{k=1}^N \sum_{j=1}^M \left\| p_t^{j,k} - \tilde{p}_t^{j,k}(\xi_i) \right\|^2, \quad (10)$$

with the corresponding featured image point number $j = 1, 2, \dots, M$, the captured image number $k = 1, 2, \dots, N$, and the optimization parameter vector $\xi_1 = \{fx, fy, \alpha, \beta, \Phi\}$. $p_t^{j,k}$ is the observation of marker j for position k . It should be noted that the parameters of the principal point and distortion are not involved in this optimization. Moreover, the minimizations in this step and hereinafter are performed by means of a suitable version of the Levenberg-Marquardt algorithms.

Step 3. Estimation of the principal points of two individual cameras. A similar objective function as in Step 2 is performed, while the optimization parameters are supposed to be changed into $\xi_2 = \{fx, fy, C_x, C_y, \Phi\}$. Likewise, the Scheimpflug angles and distortion coefficient parameters are excluded from optimization this time.

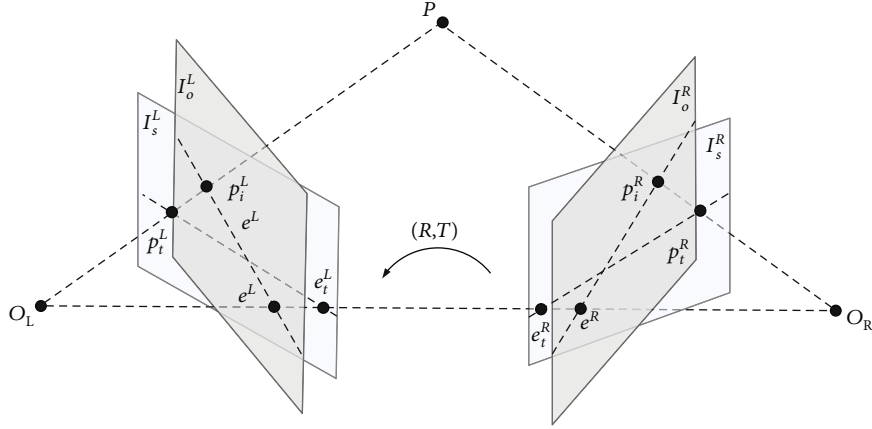


FIGURE 2: Schematic of epipolar geometry of stereo Scheimpflug cameras.

Step 4. Determination of the distortion coefficients. Given the results obtained from the previous steps, the distortion parameters are taken into consideration in this step. And the optimization parameters are supposed to be $\xi_3 = \{fx, fy, k_1, k_2, p_1, p_2, \Phi\}$.

Consequently, the intrinsic parameter vector η , including $\{fx, fy, \alpha, \beta, Cx, Cy, k_1, k_2, p_1, p_2\}$, of the two cameras can be acquired through the separated stepwise calibration procedure.

Step 5. Calculation of the relative orientation $\hat{\mathbf{R}}(\gamma, \kappa, \theta)$ and position $\hat{\mathbf{T}}(t_x, t_y, t_z)$ between the two cameras. Suppose that the optimized intrinsic and extrinsic parameter sets of two individual cameras are defined as η_l, η_r and Φ_l, Φ_r , respectively. Without loss of generality, the left camera is assumed to be the reference camera. Hence, initialization of the right camera pose with respect to the left can be expressed as

$$\begin{aligned} \hat{\mathbf{R}} &= \mathbf{R}_l^k (\mathbf{R}_r^k)^{-1}, \\ \hat{\mathbf{T}} &= \mathbf{T}_l^k - \mathbf{R}_l^k (\mathbf{R}_r^k)^{-1} \mathbf{T}_r^k. \end{aligned} \quad (11)$$

Thus, the previous results can be merged in the reference coordinate system, on the basis of which an additional optimization is implemented.

$$\rho'_i = \min \sum_{l=1}^2 \sum_{k=1}^N \sum_{j=1}^M \left\| p_t^{jkl} - \tilde{p}_t^{jkl}(\xi_i) \right\|^2, \quad (12)$$

where l refers to the number of cameras. And the optimization parameter vector converts into $\xi_4 = \{\gamma, \kappa, \theta, t_x, t_y, t_z, \Phi_l, \Phi_r\}$. Note that the optimized intrinsic parameters set η_l, η_r is employed for the optimization. Hence, all the intrinsic and extrinsic parameters of the stereo Scheimpflug cameras have been obtained.

3. Stereo-DIC with Scheimpflug Cameras

To accurately determine the full-field surface displacement and strain of the specimen, the well-developed subset-based DIC algorithms are utilized to register the images of the specimen coated with a random speckle pattern in the reference and deformed states and to match the same region between the stereo images. Typically, a square reference subset centered at the predefined calculation point is chosen from the left reference image and employed to search its corresponding location in the right image. To this end, a robust zero-mean normalized sum of squared difference (ZNSSD) criterion [27], integrated with a second-order shape function [28], is adopted to quantitatively assess the similarity between the reference and target subsets. To enhance subpixel registration accuracy, the state-of-the-art inverse compositional Gauss-Newton (IC-GN) algorithm [29] and a biquintic B-spline interpolation scheme are utilized. Giving top priority to the accuracy rather than efficiency, the matching strategy adopted here is to correlate all the deformed images of the stereo rig to the left reference image [4].

Therefore, the desired disparity data of the region of interest (ROI) can be obtained. Together with the precalibrated parameters of the stereo Scheimpflug cameras, the 3D world coordinates of the measurement points on the specimen surface can be recovered via the tailored bundle adjustment-based stereo triangulation. It should be noted that the lens distortion must be taken into consideration during the triangulation process. Furthermore, the three displacement components, resulting from external loading, can be calculated by subtracting the 3D coordinates of the same interest points at the initial state from those of the deformed. In common with literature [30], a variation of the triangular Cosserat point element method proposed in [31] is utilized to calculate the full-field strain distribution. It is worth noting that the average rigid-body motion of the specimen should be subtracted to give a better insight into the relative deformation of the specimen surface.

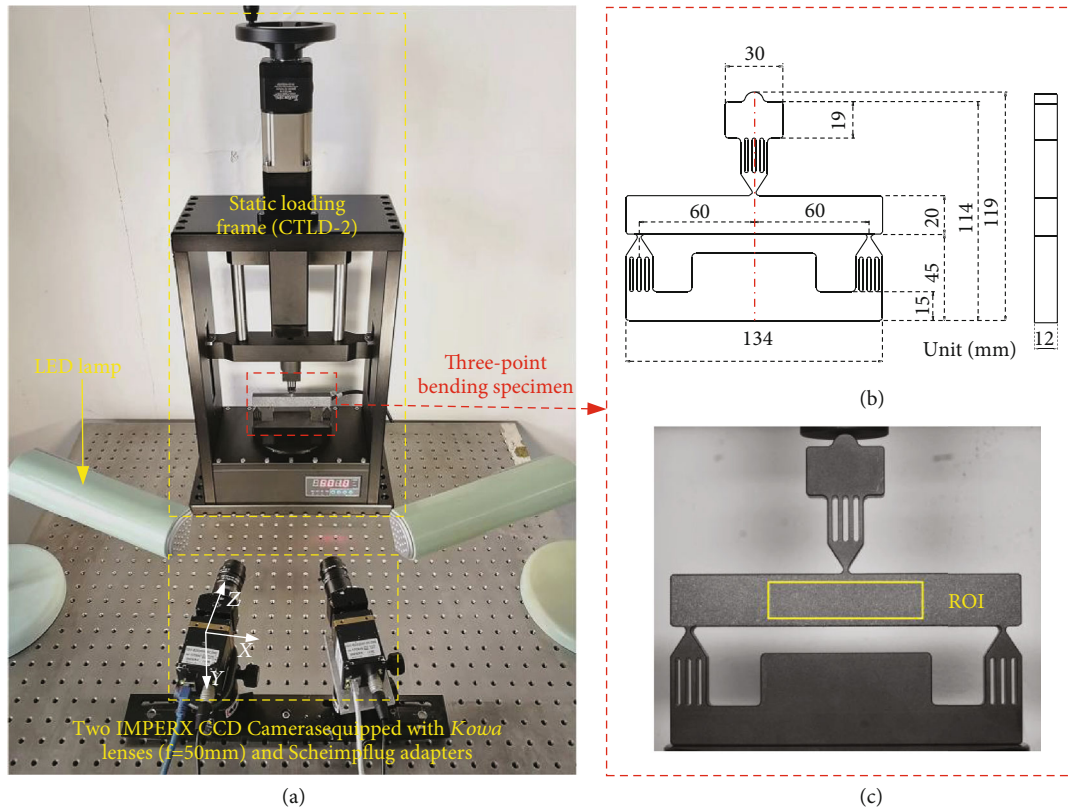


FIGURE 3: (a) Experimental setup for the three-point bending test; (b) specimen geometry; (c) ROI on the specimen surface (yellow rectangle).

4. Experiment Verification

4.1. Experimental Apparatus. To verify the performance of the developed Scheimpflug camera-based stereo-DIC system, a series of experiments, including stereo calibration of Scheimpflug cameras, rigid motion tests, and three-point bending tests of the specimen, were performed under controlled laboratory conditions.

As shown in Figure 3(a), experiments in this study have been conducted with a wide range of system configurations, which mainly include (1) two 8-bit IMPERX CCD Cameras (IGV-B2520M-SC000) employed to simultaneously record the images of the specimen surface from two directions, which have the spatial resolution of 2456×2058 pixels, and equipped with Kowa lenses (focal length 50 mm) and custom-made Scheimpflug adapters, (2) a static loading frame (CTLD-2) of 2 kN capacity, (3) a high-precision vertical linear stage (Newport GTS30V) with the precision of $0.1 \mu\text{m}$, and (4) a customized aluminum alloy three-point bending specimen, which is sketched in Figure 3(b), and the surface indicated by a yellow rectangle in the middle as depicted in Figure 3(c) is chosen as the ROI.

Note that all equipment aforementioned is mounted on a Newport optical bench, and specimen preparation consists of spraying black/white colour paint over the specimen surface to yield a suitable random speckle pattern. In order to obtain entirely focused images with small distortions, the cameras and lenses are adjusted with the aid of the Scheimpflug arrangement. Besides, uniform illumination of the specimen

surface is guaranteed via holding two LED lamps on each side of the camera. Moreover, the specially tailored experimental data processing software is developed on the basis of the well-developed open-source toolbox Ncorr [32] and Multi-DIC [30].

An example is presented in Figure 4 to compare the imaging performance of the Scheimpflug camera with that of the conventional camera under the same experimental configuration. The conventional camera here refers to the same cameras indicated in Figure 3(a) but without tilting the lens. Figures 4(a) and 4(b), respectively, show the specimen surface image obtained from the left camera based on the Scheimpflug imaging model and that based on the conventional pinhole imaging model; meanwhile, the enlarged local images are depicted on their right.

As illustrated in Figure 4(b), it is apparent that a larger range of sharp images of the ROI on the specimen surface can be acquired using the Scheimpflug camera. Besides, an effective global parameter (Mean Intensity Gradient (MIG)) [33] is adopted to further quantitatively assess the overall quality of the obtained speckle patterns. Twenty image pairs obtained via the Scheimpflug camera and the conventional camera are utilized for comparisons, and the MIG of captured speckle patterns from the Scheimpflug camera (16.8765) is obviously higher than that from the conventional camera (8.7836), which indicates that the Scheimpflug camera accordingly produces the smaller mean bias error and standard deviation error in the further DIC measurements. Thus, it can be deduced that the imaging

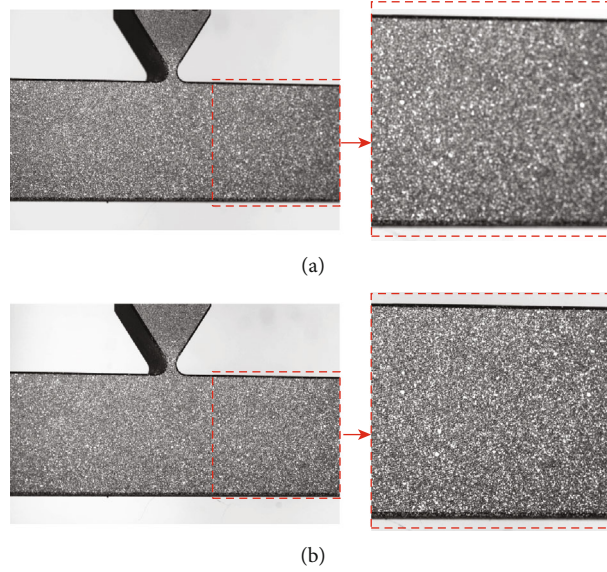


FIGURE 4: (a) The specimen surface image obtained by the conventional camera; (b) the specimen surface image obtained by the Scheimpflug camera.

performance of the Scheimpflug camera, under the experimental configuration in this paper, is superior to that of the conventional camera.

4.2. Stereo Scheimpflug Camera Calibration. Prior to specimen testing, the Scheimpflug camera-based stereo-DIC system should be well calibrated. As sketched in Figure 3(a), two Scheimpflug cameras are symmetrically arranged, with the normal to the specimen surface such that it approximately bisects the stereo angle. In the calibration experiment, a printed checkerboard pattern attached to a cardboard rather than high-precision calibration targets is adopted. The calibration pattern consists of a plane of $12 * 9$ grids with 5 mm checkerboard spacing. Totally, 30 images of the checkerboard under different orientations and positions are captured. Employing the proposed stepwise stereo camera calibration technique, the intrinsic and extrinsic parameters, as well as the reprojection errors of the stereo rig, can be retrieved in Table 1.

To further verify the calibration results of the Scheimpflug rig, the 3D coordinates and structure of 20 arbitrarily placed checkerboards are reconstructed via the rig with the calibrated parameters and simultaneously obtained image pairs. And we fit the reconstructed coordinates with an ideal flat plane and calculated the distance between the reconstructed points and the ideal plane. Moreover, a typical reconstruction result is given in Figure 5.

Figure 5(a) depicts the reconstructed 3D checkerboard points and the fitted plane while the error distribution of the reconstructed checkerboard points is presented in Figure 5(b). As indicated in Figure 5(a), the reconstructed 3D points agree well with the fitted plane in spite of minor deviations. Furthermore, it can be found out in Figure 5(b) that the deviations of reconstructed points are approximately symmetrical about the center of the fitted plane, while the deviations at the corners are more significant. Nonetheless, the maximum deviation of the reconstructed points is

TABLE 1: The calibration results of the Scheimpflug stereo cameras.

Intrinsic parameters	Left camera	Right camera
f_x	10912.3651	10025.7085
f_y	10896.6062	10977.6092
α ($^\circ$)	0.6156	0.3511
β ($^\circ$)	-4.5583	4.4574
C_x	868.9786	1503.2014
C_y	989.9657	1000.1329
k_1	-0.3621	-0.3208
k_2	0.8389	1.3490
p_1	-0.0013	-0.0022
p_2	-0.0108	-0.0104
Reprojection error (pixel)	0.3479	0.3528
R (in Rodriguez form)	(0.0037, 0.3948, -0.0115)	
T (mm)	(-144.8040, 1.3722, 27.9974)	

approximately 0.030 mm, which is still quite small compared with the depth of the checkerboard. Besides, the RMSE (Root Mean Squared Error) of the distance between all the reconstructed 3D points and the corresponding fitted planes under 20 different poses is 0.0133 mm. Consequently, the experimental results verify the effectiveness and accuracy of the calibration method.

4.3. Rigid-Body Motion Test. To quantify the metrological performance of the developed Scheimpflug camera-based stereo-DIC system, a null strain test was performed on the specimen subjected to a rigid-body motion [34]. As these fields are theoretically equal to zero, we can thus obtain the overall error of the displacement measurements. The three-point bending specimen is positioned on the high-precision

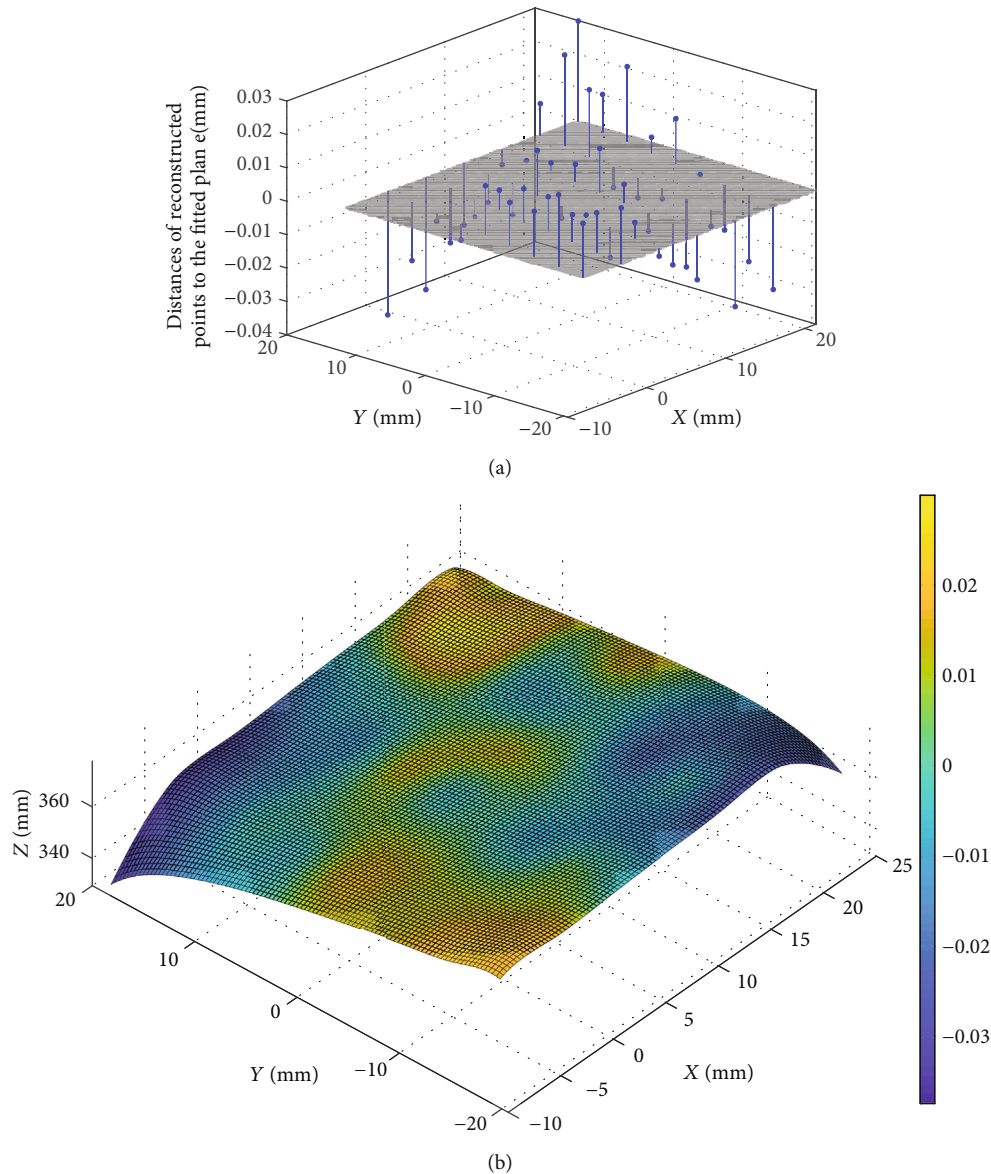


FIGURE 5: (a) The reconstructed 3D checkerboard points and the fitted 3D plane; (b) the error distribution of the reconstructed points with respect to the fitted plane.

vertical linear stage, and the stage is moved along the vertical direction from 0 to 10 mm and back to 0 mm by steps of 1 mm with regard to the reference position. Stereo images are simultaneously captured for each position of the specimen. According to the criterion developed in [35], a subset size of $64 * 64$ pixels coupled with a step size of 5 pixels is chosen during the stereo-DIC processing; therefore, the full-field displacements and strains of the specimen surface can be calculated.

Given that the reference frame of the vertical linear stage is not identical to the reference frame of the proposed stereo-DIC system, the scale of the displacement $D = \sqrt{X^2 + Y^2 + Z^2}$, rather than the 3D (X, Y, Z) displacement components, is compared between the proposed stereo-DIC measurements and the readout of the vertical linear stage.

As shown in Figure 6(a), the average displacement measurements of the specimen are compared with reference values obtained from the vertical linear stage, and the corresponding standard deviation of displacements is illustrated in Figure 6(b).

It can be observed that the displacement measurements for the Scheimpflug-based stereo-DIC system is in well conformity with the reference imposed vertical displacements. It is worth noting that as the imposed vertical displacements increase from 1 to 10 mm, the average errors of the measured specimen displacements are enlarged from $5.8 \mu\text{m}$ (unit of micron) to $50.9 \mu\text{m}$. In the meanwhile, the standard deviations of the specimen climb from $1.9 \mu\text{m}$ to $10.3 \mu\text{m}$. Despite all these, the average errors and standard deviations of displacement measurements are rather low, even in the case

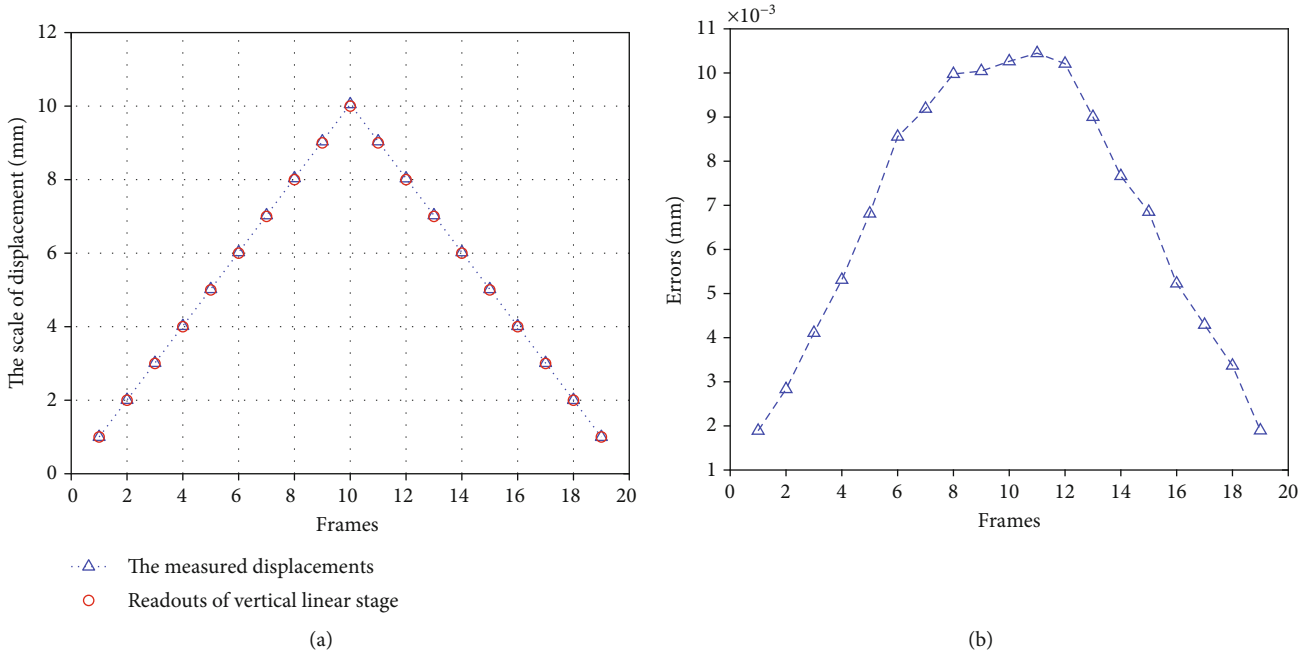


FIGURE 6: (a) The scale of the specimen displacements measured by the proposed method against reference values; (b) the standard deviation of the specimen displacements related to the vertical translations.

of large vertical translations. As the translation is increased, the percent of average errors and standard deviations in displacement measurements has remained approximately constant. Consequently, these results indicate that the displacement measurement for the Scheimpflug-based stereo-DIC system is fairly accurate.

4.4. Three-Point Bending Experiment. To further verify the validity of the proposed method, a three-point bending experiment is performed on the specially customized specimen, which is widely adopted to identify the flexural and tensile strength of quasibrittle materials. The experimental setup is exhibited in Figure 3, the specimen is positioned on the center of the loading frame, and a pair of images captured at a small load (about 20 N) is taken as the reference configuration. It needs to be emphasized that the small load applied here is to overcome excessive rigid-body motion due to any slack in loading fixtures [36]. As the applied load increases from 20 up to 2000 N with the increment of 200 N, a series of image pairs are recorded as the deformed configuration. The same settings as in the rigid-body motion test are applied to the subset-based matching operation. Therefore, full-field distributions of the specimen surface displacement and deformation can be obtained and utilized to explain the underlying deformation mechanisms in the three-point bending test. Moreover, Figures 7(a)–7(c), respectively, depict the typical evolution of full-field distributions of displacement components in three directions along with the increase in the applied load (left 600 N, middle 1200 N, and right 1800 N).

It is worthwhile to notice that all the experimental results in this paper are obtained in the left camera coordinate sys-

tem. As shown in Figure 3(a), the Z-axis points to the specimen surface, while the Y-axis is vertically downward and the X-axis forms a right-hand coordinate system. Even though the small angle between the Z-axis and the normal of the specimen surface exists, for convenience of analysis, it is ignored and assumed that the Z-axis is perpendicular to the specimen surface, while the X-axis and Y-axis are, respectively, parallel to the longitudinal and transverse directions of the ROI. Namely, the static loading direction is approximately parallel to the Y-axis.

Globally, displacement maps of the components in three directions in Figures 7(a)–7(c) exhibit typical patterns that are characteristics of three-point bending tests. As illustrated in Figure 7(a), the displacement fields of the X-components are distributed symmetrically in the center and the displacements in the middle part of the specimen surface are relatively low and gradually increase towards both ends of the specimen surface. With the increase in the applied loads, the upper surface of the specimen tends to move towards the middle, while the lower surface moves towards the opposite direction. As for Y-components in Figure 7(b), they are axially symmetrically distributed, and the middle parts of the specimen surface move downward along the Y-axis, while the sides move upward. In the case of the displacements of Z-components, they are much smaller than those in the other two directions. In general, the displacements at the edge of the specimen surface are larger than those at the central part. Actually, for the arrangement in these experiments, the displacements of Z-components can be approximated as the out-of-plane displacements on the specimen surface. Moreover, Figure 7(d) shows the full-field distribution of the specimen surface displacement magnitude. It

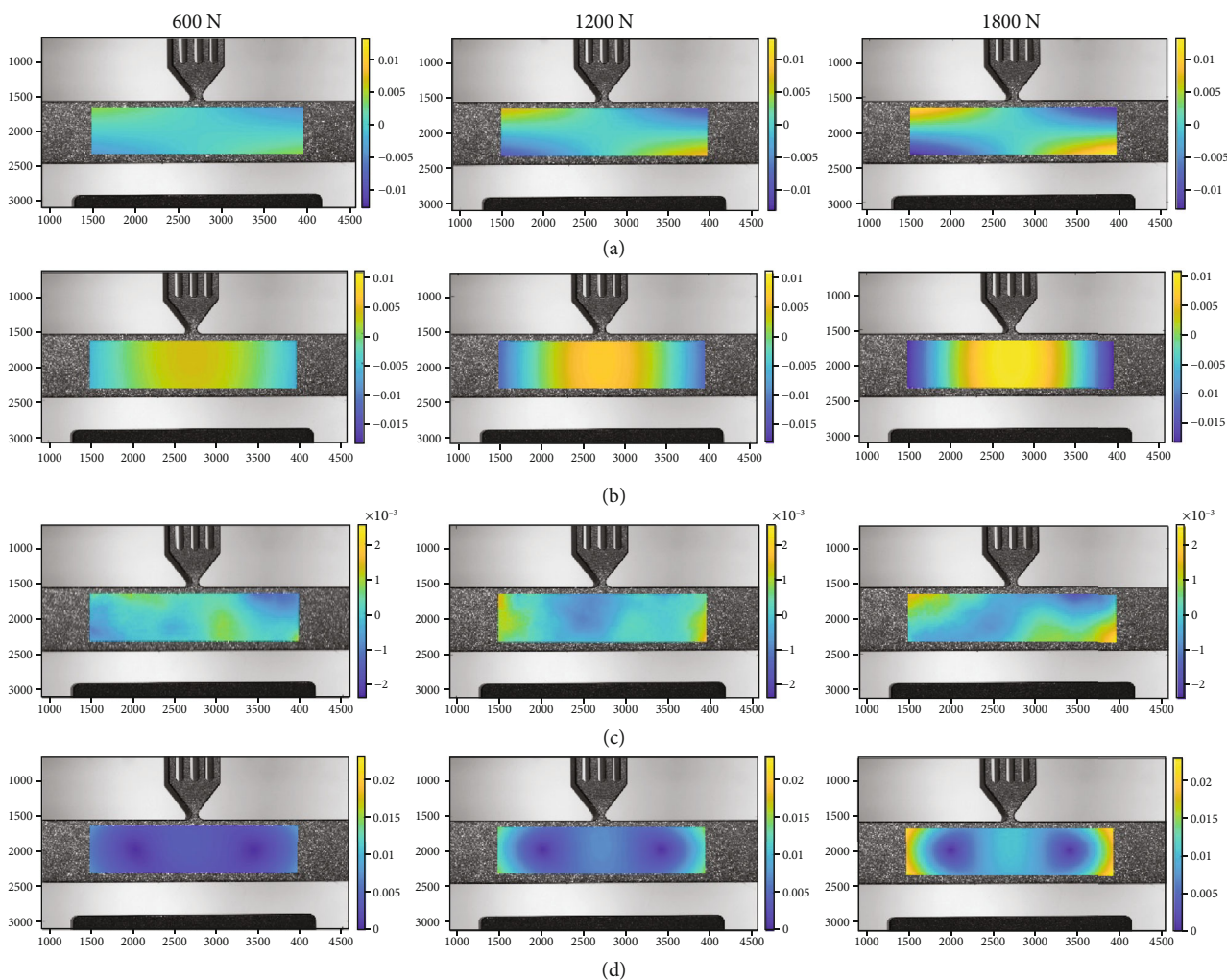


FIGURE 7: The full-field distribution of the specimen surface displacement components and magnitude at selected loads (unit (mm)): (a) X-component displacements; (b) Y-component displacements; (c) Z-component displacements; (d) displacement magnitude.

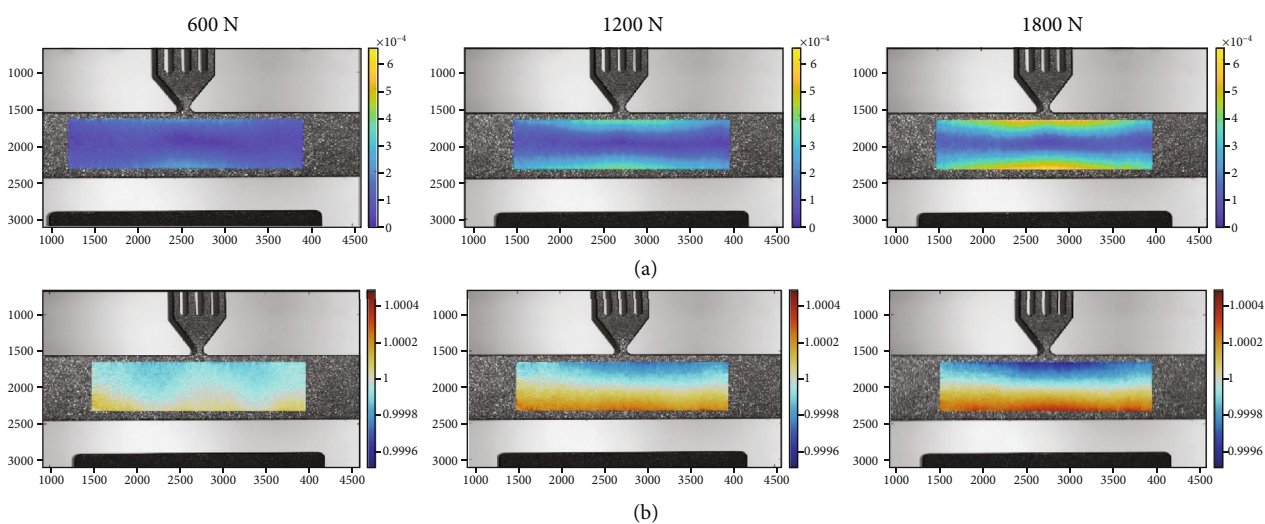


FIGURE 8: (a) The full-field distribution of Lagrangian strain magnitude maps at given loads; (b) the relative area change of the specimen surface at given loads.

can be observed that two fixed minimum points appear between the three loading heads and do not change as the applied loads increase.

Besides, the full-field distribution of Lagrangian strain magnitude maps corresponding to the typical applied loads is shown in Figure 8(a); meanwhile, Figure 8(b) illustrates the relative surface area change of the specimen. It can be found that the strain mainly occurs at the upper and lower parts of the specimen surface, while the strain on the neutral plane is rather close to zero. Further, as revealed in Figure 8(b), the upper surface area of the specimen is compressed while the lower surface area is stretched, and this trend is more pronounced as the applied load increases. Considering the geometric size of the aluminum alloy specimen and the limited capacity of the static loading frame, the deformation and strain levels of the specimen are relatively small. Despite all that, the experimental results of three-point bending further validate the effectiveness of the proposed method. Further analysis of the specimen's mechanical properties is beyond the scope of this work but can be found in [37].

5. Conclusions

In this article, a novel Scheimpflug camera-based stereo-DIC method is developed for the full-field 3D shape and deformation measurement. In contrast with conventional cameras, the Scheimpflug camera enables extending the measurement range of the stereo-DIC system without zooming the aperture, which exhibits significant advantages over conventional cameras in stereo-DIC measurements. Also, a robust and effective stepwise calibration approach is presented to calculate the intrinsic and extrinsic parameters of the stereo Scheimpflug rig. Consequently, with the aid of the tailored stereo triangulation method and well-developed subset-based DIC algorithms, the three-dimensional shape and deformation of the specimen can be retrieved. Finally, experimental results of rigid-body motion tests and three-point bending tests successfully demonstrate the accuracy and effectiveness of the proposed approach. Due to the attractive advantages of employing Scheimpflug cameras, the proposed technique offers new avenues for performing 3D deformation measurements and indicates great potentials in further fields of stereo-DIC measurements.

Data Availability

The data used to support the findings of this study are available from the corresponding author upon request.

Conflicts of Interest

The authors declare that there is no conflict of interest regarding the publication of this paper.

Acknowledgments

This research was funded by the National Natural Science Foundation of China (NSFC) under Grant Nos. 11872070, 11727804, and 11902349.

References

- [1] Z. L. Kahn-Jetter and T. C. Chu, "Three-dimensional displacement measurements using digital image correlation and photogrammic analysis," *Experimental Mechanics*, vol. 30, no. 1, pp. 10–16, 1990.
- [2] P. F. Luo, Y. J. Chao, M. A. Sutton, and W. H. Peters III, "Accurate measurement of three-dimensional deformations in deformable and rigid bodies using computer vision," *Experimental Mechanics*, vol. 33, no. 2, pp. 123–132, 1993.
- [3] M. A. Sutton, F. Matta, D. Rizos et al., "Recent progress in digital image correlation: background and developments since the 2013 W M Murray Lecture," *Experimental Mechanics*, vol. 57, no. 1, pp. 1–30, 2017.
- [4] B. Pan, "Digital image correlation for surface deformation measurement: historical developments, recent advances and future goals," *Measurement Science and Technology*, vol. 29, no. 8, article 082001, 2018.
- [5] O. De Almeida, F. Lagattu, and J. Brillaud, "Analysis by a 3D DIC technique of volumetric deformation gradients: application to polypropylene/EPR/talc composites," *Composites Part A: Applied Science and Manufacturing*, vol. 39, no. 8, pp. 1210–1217, 2008.
- [6] M. Palanca, G. Tozzi, and L. Cristofolini, "The use of digital image correlation in the biomechanical area: a review," *International Biomechanics*, vol. 3, no. 1, pp. 1–21, 2016.
- [7] T. A. Berfield, J. K. Patel, R. G. Shimmin, P. V. Braun, J. Lambros, and N. R. Sottos, "Micro- and nanoscale deformation measurement of surface and internal planes via digital image correlation," *Experimental Mechanics*, vol. 47, no. 1, pp. 51–62, 2007.
- [8] L. Tian and B. Pan, "Remote bridge deflection measurement using an advanced video deflectometer and actively illuminated LED targets," *Sensors*, vol. 16, no. 9, article 1344, 2016.
- [9] L. Yu and B. Pan, "Full-frame, high-speed 3D shape and deformation measurements using stereo- digital image correlation and a single color high-speed camera," *Optics and Lasers in Engineering*, vol. 95, pp. 17–25, 2017.
- [10] B. Pan, L. Yu, and D. Wu, "Thermo-mechanical response of superalloy honeycomb sandwich panels subjected to non-steady thermal loading," *Materials & Design*, vol. 88, pp. 528–536, 2015.
- [11] J.-J. Orteu, F. Bugarin, J. Harvent, L. Robert, and V. Velay, "Multiple-camera instrumentation of a single point incremental forming process pilot for shape and 3D displacement measurements: methodology and results," *Experimental Mechanics*, vol. 51, no. 4, article 9436, pp. 625–639, 2011.
- [12] Y. Wang, P. Lava, S. Coppieters, P. V. Houtte, and D. Debruyne, "Application of a multi-camera stereo DIC set-up to assess strain fields in an Erichsen test: methodology and validation," *Strain*, vol. 49, no. 2, pp. 190–198, 2013.
- [13] F. Chen, X. Chen, X. Xie, X. Feng, and L. Yang, "Full-field 3D measurement using multi-camera digital image correlation system," *Optics and Lasers in Engineering*, vol. 51, no. 9, pp. 1044–1052, 2013.
- [14] M. Malesa, K. Malowany, J. Pawlicki et al., "Non-destructive testing of industrial structures with the use of multi-camera digital image correlation method," *Engineering Failure Analysis*, vol. 69, pp. 122–134, 2016.
- [15] D. Calluau and L. David, "Stereoscopic particle image velocimetry measurements of the flow around a surface-mounted block," *Experiments in Fluids*, vol. 36, no. 1, pp. 53–61, 2004.

- [16] J. Li, Y. Guo, J. Zhu et al., "Large depth-of-view portable three-dimensional laser scanner and its segmental calibration for robot vision," *Optics and Lasers in Engineering*, vol. 45, no. 11, pp. 1077–1087, 2007.
- [17] A. Miks, J. Novak, and P. Novak, "Analysis of imaging for laser triangulation sensors under Scheimpflug rule," *Optics Express*, vol. 21, no. 15, pp. 18225–18235, 2013.
- [18] H. M. Merklinger, *Focusing the View Camera: A Scientific Way to Focus the View Camera and Estimate Depth of Field*, 2010.
- [19] P. Berliner, *The Scheimpflug Principle*, Projection Lights & Staging News, 2010.
- [20] Z. Zhang, "A flexible new technique for camera calibration," *IEEE Transactions on Pattern Analysis and Machine Intelligence*, vol. 22, no. 11, pp. 1330–1334, 2000.
- [21] A. Legarda, A. Izaguirre, N. Arana, and A. Iturrospe, "A new method for Scheimpflug camera calibration," in *2011 10th International Workshop on Electronics, Control, Measurement and Signals*, Liberec, Czech Republic, 2011.
- [22] H. Louhichi, T. Fournel, J. M. Lavest, and H. B. Aissia, "Self-calibration of Scheimpflug cameras: an easy protocol," *Measurement Science and Technology*, vol. 18, pp. 2616–2622, 2007.
- [23] O. Albers, A. Poesch, and E. Reithmeier, "Flexible calibration and measurement strategy for a multi-sensor fringe projection unit," *Optics Express*, vol. 23, pp. 29592–29607, 2015.
- [24] C. Steger, "A comprehensive and versatile camera model for cameras with tilt lenses," *International Journal of Computer Vision*, vol. 123, no. 2, pp. 121–159, 2017.
- [25] P. Cornic, C. Illoul, A. Cheminet et al., "Another look at volume self-calibration: calibration and self-calibration within a pinhole model of Scheimpflug cameras," *Measurement Science and Technology*, vol. 27, no. 9, article 094004, 2016.
- [26] C. Sun, H. Liu, M. Jia, and S. Chen, "Review of calibration methods for Scheimpflug camera," *Journal of Sensors*, vol. 2018, Article ID 3901431, 15 pages, 2018.
- [27] B. Pan, H. Xie, and Z. Wang, "Equivalence of digital image correlation criteria for pattern matching," *Applied Optics*, vol. 49, no. 28, pp. 5501–5509, 2010.
- [28] B. Wang and B. Pan, "Random errors in digital image correlation due to matched or overmatched shape functions," *Experimental Mechanics*, vol. 55, no. 9, pp. 1717–1727, 2015.
- [29] B. Pan, K. Li, and W. Tong, "Fast, robust and accurate digital image correlation calculation without redundant computations," *Experimental Mechanics*, vol. 53, no. 7, pp. 1277–1289, 2013.
- [30] D. Solav, K. M. Moerman, A. M. Jaeger, K. Genovese, and H. M. Herr, "MultiDIC: an open-source toolbox for multi-view 3D digital image correlation," *IEEE Access*, vol. 6, pp. 30520–30535, 2018.
- [31] D. Solav, M. B. Rubin, A. Cereatti, V. Camomilla, and A. Wolf, "Bone pose estimation in the presence of soft tissue artifact using triangular Cosserat point elements," *Annals of Biomedical Engineering*, vol. 44, no. 4, pp. 1181–1190, 2016.
- [32] J. Blaber, B. Adair, and A. Antoniou, "Ncorr: open-source 2D digital image correlation Matlab software," *Experimental Mechanics*, vol. 55, no. 6, pp. 1105–1122, 2015.
- [33] B. Pan, Z. Lu, and H. Xie, "Mean intensity gradient: an effective global parameter for quality assessment of the speckle patterns used in digital image correlation," *Optics and Lasers in Engineering*, vol. 48, no. 4, pp. 469–477, 2010.
- [34] H. Haddadi and S. Belhabib, "Use of rigid-body motion for the investigation and estimation of the measurement errors related to digital image correlation technique," *Optics and Lasers in Engineering*, vol. 46, no. 2, pp. 185–196, 2008.
- [35] B. Pan, H. Xie, Z. Wang, K. Qian, and Z. Wang, "Study on subset size selection in digital image correlation for speckle patterns," *Optics Express*, vol. 16, no. 10, pp. 7037–7048, 2008.
- [36] D. Lee, H. Tippur, and P. Bogert, "Quasi-static and dynamic fracture of graphite/epoxy composites: an optical study of loading-rate effects," *Composites Part B: Engineering*, vol. 41, no. 6, pp. 462–474, 2010.
- [37] G. Morada, A. Vadean, and R. Boukhili, "Failure mechanisms of a sandwich beam with an ATH/epoxy core under static and dynamic three-point bending," *Composite Structures*, vol. 176, pp. 281–293, 2017.
- [38] J. Weng, P. Cohen, and M. Herniou, "Camera calibration with distortion models and accuracy evaluation," *IEEE Transactions on Pattern Analysis and Machine Intelligence*, vol. 14, no. 10, pp. 965–980, 1992.



Hindawi

Submit your manuscripts at
www.hindawi.com

